Light-Weight Panoramic Mirror Design for Visual Navigation

Wolfgang Stürzl[1], Michael Suppa[2] and Darius Burschka[3]

[1] Department of Neurobiology, Bielefeld University, Germany
[2] Institute of Robotics and Mechatronics, German Aerospace Agency (DLR)
[3] Department of Informatics, Technische Universität München, Germany
wolfgang.stuerzl@uni-bielefeld.de, michael.suppa@dlr.de, burschka@cs.tum.edu

Abstract. We present a compact and light-weight panoramic lens developed to be mounted on standard off-the-shelf video cameras. Obstruction-free imaging is achieved by enclosing a reflective surface in acrylic glass whose surface is specifically designed to minimize internal reflections. Although the approach is generic and can be applied to any camera system, our special focus is on miniature cameras used on flying systems (UAVs). We present the mathematical background for the sensor model of the reflective and refractive surfaces and present an analytical analysis of the image formation in particular with respect to image blur. We show, how the sensor can be used for monocular navigation on mobile systems.

1 Introduction

Navigation systems provide basic functionality required for flexible mission planning of any robotic system. The robot kinematics, e.g., wheeled odometry is prone to measurement errors and only local maps are usually generated, which can be fused by registration [1]. In other approaches the absolute position is estimated from the generated environment models [2]. However, range images are required in order to allow for registration. Furthermore, wheeled odometry requires physical contact to the ground which is not available for flying systems. Hence, inertial measurement units are commonly used to estimate the pose of flying robots. However, to account for drift they require additional information, often by using GPS, which is not suitable for indoor navigation.

In particular for autonomously flying systems, vision provides crucial information that can be used, for example, to stabilize flight, detect objects and avoid obstacles. Having omni-directional vision is advantageous for the estimation of ego-motion [3] and on systems that can fly in all directions, e.g. a multi-rotor system [4]. It can also be beneficial for the recognition of places since the whole scene is visible independent of flight direction or camera orientation [5–7]. In this paper we present a light-weight and compact panoramic vision system, especially suited for small UAVs. In addition to an in-depth analysis of the system's imaging properties, we show its application to robust visual navigation.

Workshop Proceedings of SIMPAR 2008
Intl. Conf. on SIMULATION, MODELING and PROGRAMMING for AUTONOMOUS ROBOTS
Venice(Italy) 2008 November,3-4
ISBN 978-88-95872-01-8
pp. 218-229

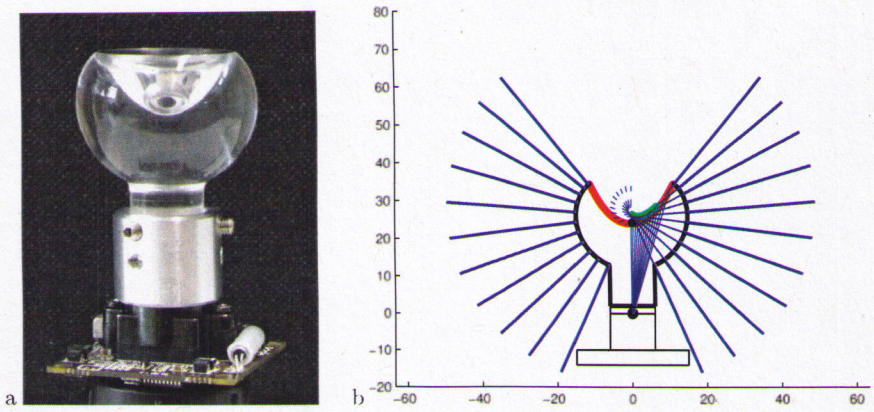

Fig. 1. a) Picture of the vision system which weighs about 33 g. Total height is approx. 50 mm. The diameter of the perspex globe (weight $\approx$ 13 g) is approx. 30 mm. The small board camera is a standard PAL camera equipped with a 3.6 mm lens (weight of camera including lens $\approx$ 14 g). The camera lens is hidden inside the bracket that holds the perspex body (weight of bracket is approx. 6 g which can be easily reduced). b) Drawing of the system and ray tracing (cross-section). The reflective surface is highlighted in red. The thick green curve shows the caustic of viewpoints. The black dot at the apex of the mirror surface depicts the position of the approximated "single viewpoint" (see section 2.3).

2 Description of the Imaging System

The main features of the imaging device presented in this paper are (1) obstruction-free panoramic vision with at least $[-55°, +45°]$ of useable elevation range, and (2) a rugged but light-weight and small design (total weight less than 33 g, diameter $\lesssim$ 30 mm) that minimizes internal reflections.

A picture of the optical system which is machined from solid perspex is shown in Fig. 1 a. As depicted in Fig. 1 b, light rays enter the vision system through a curved perspex surface before being reflected at a mirror surface. Rays are then refracted into the lens of the video camera through a planar perspex surface. Examples of camera images are shown in Fig. 4. In the following sections we describe the design and the properties of the optical system.

2.1 Shape of Reflective Surface

The reflective surface of the optical system is a "constant angular gain mirror" described in [8]. Such surfaces have a linear relation ship between the angle of incidence on the reflective surface and the camera angle and thus give an almost constant angular resolution along radial directions in the camera image. They also can provide very large fields of view but do not have a single viewpoint unlike the mirror shapes presented in [9]. As depicted in Fig. 2 b, the reflective

Workshop Proceedings of SIMPAR 2008
Intl. Conf. on SIMULATION, MODELING and PROGRAMMING for AUTONOMOUS ROBOTS
Venice(Italy) 2008 November,3-4
ISBN 978-88-95872-01-8
pp. 218-229

surface is defined by

$$\boldsymbol{x}(\phi,\eta) := r(\eta)\boldsymbol{e}(\phi,\eta) \ , \quad \eta \in (0,\, \eta_{\max}) \ , \tag{1}$$

$$r(\eta) := r_0 \frac{\cos^k\gamma}{\cos(\eta/k+\gamma)^k} \ , \quad k := \frac{2}{1+\alpha} \ , \tag{2}$$

$$\boldsymbol{e}(\phi,\eta) := (\cos\phi\sin\eta, \sin\phi\sin\eta, \cos\eta)^\top \ . \tag{3}$$

where ϕ is the azimuth angle, η is the angle between the incoming rays and the optical axis of the camera, r_0 is the distance from nodal point of camera to the apex of the reflective surface, γ is the tangent angle at the apex, $\eta_{\max}$ is the maximum angle covered by the reflective surface, and α is the vertical angular gain.

The parameter values for the imaging device described in this paper are $r_0 = 25\,\text{mm}$, $\gamma = 0°$, $\eta_{\max} = 17.5°$, and $\alpha = 8.25$.

Due to the refraction at the flat ending of the perspex, the reflective surface has to be mounted a bit closer to the view point of the camera than r_0. The shift is approximately $\Delta h = (1 - n_p)h \approx -0.5h$, where h is the distance of the nodal point of the camera to planar surface of the perspex and $n_p \approx 1.5$ is the refraction index of the perspex body. In our case, we have $h \approx 2\,\text{mm}$ and thus $\Delta h \approx -1\,\text{mm}$. In addition, while the reflective surface covers up to $\eta_{\max} = 17.5°$, the corresponding camera angle is $\theta_{\max} \approx n_p\eta_{\max} = 26.25°$.

2.2 Shape of Outer Perspex Surface

The outer perspex surface is designed to ensure perpendicular incidence of principal rays[4]. This preserves the constant gain property and minimizes internal reflections [10, 11]. Its shape is given by

$$\boldsymbol{s}(\phi,\eta) := r(\eta)\boldsymbol{e}(\phi,\eta) + (r_{\max} - r(\eta))\boldsymbol{e}_o(\phi,\eta) \ , \tag{4}$$

$$r_{\max} := r(\theta_{\max}) \approx 37.3\,\text{mm} \ , \tag{5}$$

$$\boldsymbol{e}_o(\phi,\eta) := (\cos\phi\sin(\alpha\eta+2\gamma), \sin\phi\sin(\alpha\eta+2\gamma), -\cos(\alpha\eta+2\gamma))^\top \ . \tag{6}$$

See [10] for the derivation of Eq. (4).

2.3 Viewpoints and Calibration

The caustic surface of viewpoints of a constant gain mirror was already derived in [12] using the approach described in [13, 14] (see [15] for a geometric approach),

$$\mathbf{c}(\phi,\eta) := r(\eta)\,(\cos\phi\, f_\rho(\eta), \sin\phi\, f_\rho(\eta), f_z(\eta))^\top \ , \tag{7}$$

$$f_\rho(\eta) := \sin\eta - 1/\alpha\sin(\alpha\eta+2\gamma) \ , \tag{8}$$

$$f_z(\eta) := \cos\eta + 1/\alpha\cos(\alpha\eta+2\gamma) \ . \tag{9}$$

[4] principal rays are rays that enter the camera through the nodal point of its lens.

Workshop Proceedings of SIMPAR 2008
Intl. Conf. on SIMULATION, MODELING and PROGRAMMING for AUTONOMOUS ROBOTS
Venice(Italy) 2008 November,3-4
ISBN 978-88-95872-01-8
pp. 218-229

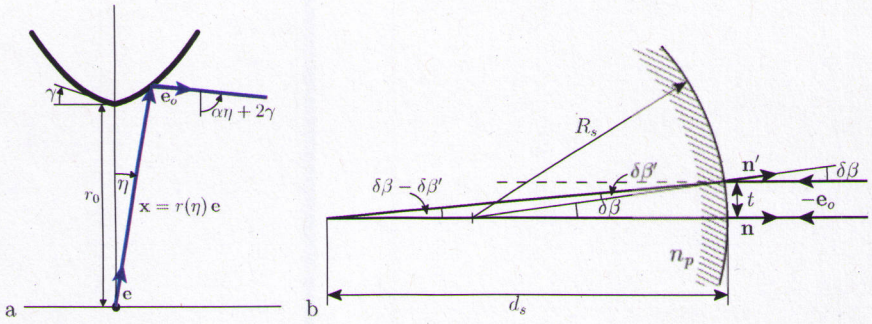

Fig. 2. a) Parameters used in Eqs. (1), (2) to describe a reflective surface with constant vertical angular gain α. Rays starting from the nodal point of the camera with angle η have, after reflection at the reflective surface, the angle $\eta' = \pi - (\alpha\eta + 2\gamma)$, i.e. $|\partial\eta'/\partial\eta| = \alpha$. The corresponding direction vectors are $\boldsymbol{e}$ and $\boldsymbol{e}_o$, defined in Eqs. (3) and (6). b) Refraction of parallel rays at a curved surface: The central ray and another ray (shifted by t) intersect, after refraction at the surface with curvature radius R_s, at distance d_s from the surface. Since $t \approx R_s\delta\beta \approx d_s\,(\delta\beta - \delta\beta')$, and $n_p\delta\beta' \approx \delta\beta$ (law of refraction), we obtain $d_s \approx R_s(1 - 1/n_p)^{-1}$ which is exact as t approaches 0.

The green curve in Fig. 1 b shows a vertical transect of $\mathbf{c}(\phi, \eta)$ for our imaging system. Although it is strictly speaking not a single view-point system, this will be noticeable only for very close objects, since the caustic of view-points is confined to a small region, and using a fixed point at (0, 24 mm) close to the tip of the reflective surface (see Fig. 1 b), all rays have distances smaller than 2.5 mm to this approximated view-point. Thus for calibration, we decided to use the publicly available Matlab "OcamCalib" toolbox that is based on a single viewpoint calibration model [16]. A calibration method with a non-central model is described in [17].

2.4 Manufacturing

The perspex body was machined on a CNC lathe[5] and then hand-polished on a lathe. Next, an aluminum layer was vapor deposited[6], and finally the perspex body was attached to a small PAL-camera using a custom-made bracket[7], see Fig. 1 a.

3 Image Formation and Camera Focus

In this section, we analyze the image formation properties of the vision sensor by considering a thin bundle of incoming parallel rays from a distant object

[5] Thanks to DLR mechanics workshop.
[6] At company Befort Wetzlar (`www.befort-optic.com`).
[7] Thanks to mechanics workshop at Bielefeld University.

Workshop Proceedings of SIMPAR 2008
Intl. Conf. on SIMULATION, MODELING and PROGRAMMING for AUTONOMOUS ROBOTS
Venice(Italy) 2008 November,3-4
ISBN 978-88-95872-01-8
pp. 218-229

that is transformed by the refractive and reflective surfaces. The analysis that is based on local curvatures and Taylor expansion, provides – unlike numerical or ray-tracing approaches, see e.g. [9] – analytical descriptions of the location of (virtual) images, enabling us to discuss the imaging quality of the system.

3.1 Refraction at the Outer Perspex Surface

A bundle of parallel light rays will first hit the outer surface of the perspex body. Since the central ray runs along the direction of the local normal vector, see Figs. 1 b and 2 b, the location of the image created by this surface can be estimated directly from the local curvatures. If the curvatures for different transects are not the same, even near-central rays will not intersect in a single point. This effect is maximized for rays shifted along the two principal curvature directions of the perspex surface. These two groups of rays we will consider in the following.

One can show that the principal radii of curvatures for the outer perspex surface, defined in Eq. (4), are given by[8]

$$\begin{aligned} R_{s\eta}(\eta) &= r_{\max} - r(\eta)\left(1 - \tfrac{1}{\alpha}\right) \ , \\ R_{s\phi}(\eta) &= r_{\max} - r(\eta)\left(1 - \tfrac{\sin\eta}{\sin(\alpha\eta+2\gamma)}\right) \ . \end{aligned} \tag{10}$$

Then, from the law of refraction (see Fig. 2 b), we find that near-central rays of the two groups considered intersect at distances $d_{s\eta}$ and $d_{s\phi}$ from the surface,

$$\begin{aligned} d_{s\eta}(\eta) &= \tfrac{R_{s\eta}(\eta)}{1-\frac{1}{n_p}} = \tfrac{n_p}{n_p-1}\left(r_{\max} - r(\eta)\left(1 - \tfrac{1}{\alpha}\right)\right) \ , \\ d_{s\phi}(\eta) &= \tfrac{R_{s\phi}(\eta)}{1-\frac{1}{n_p}} = \tfrac{n_p}{n_p-1}\left(r_{\max} - r(\eta)\left(1 - \tfrac{\sin\eta}{\sin(\alpha\eta+2\gamma)}\right)\right) \ , \end{aligned} \tag{11}$$

where $n_p \approx 1.5$ is the refraction index of the perspex. Distances to the mirror surface along $\boldsymbol{e}_o$ can be calculated according to

$$d_\xi(\eta) = r_{\max} - r(\eta) - d_{s\xi}(\eta) \ , \quad \xi \in \{\eta, \phi\} \ . \tag{12}$$

For the described vision sensor, we have $d_\eta(\eta), d_\phi(\eta) < 0$.

3.2 Reflection at the Mirror Surface

After refraction, the bundle of rays hits the curved reflective surface. Using an extended version of the analysis describe in [12], which is derived in the appendix, we can estimate the regions where (virtual) images are created by the mirror surface.

Again we consider two groups of light rays shifted along the principal curvature directions of the surface, but instead of parallel rays we assume that the

[8] The corresponding principal curvature directions are given by the vectors $\boldsymbol{e}_{s\eta}(\phi,\eta) := \frac{1}{\alpha}\frac{\partial}{\partial\eta}\boldsymbol{e}_o(\phi,\eta) = (\cos\phi\cos(\alpha\eta+2\gamma), \sin\phi\cos(\alpha\eta+2\gamma), \sin(\alpha\eta+2\gamma))^\top$ and $\boldsymbol{e}_{s\phi}(\phi,\eta) = \frac{1}{\sin(\alpha\eta+2\gamma)}\frac{\partial}{\partial\phi}\boldsymbol{e}_o(\phi,\eta) = (-\sin\phi, \cos\phi, 0)^\top$.

Workshop Proceedings of SIMPAR 2008
Intl. Conf. on SIMULATION, MODELING and PROGRAMMING for AUTONOMOUS ROBOTS
Venice(Italy) 2008 November,3-4
ISBN 978-88-95872-01-8
pp. 218-229

rays start from an object point that has distance d to the surface[9], measured along $\boldsymbol{e}_o$, see Fig. 3 a. As derived in the appendix and depicted in Fig. 3 a, the distance from the point where the central ray hits the reflective surface to the point where the rays meet (measured along direction $\boldsymbol{e}(\phi,\eta)$) is given by

$$\begin{aligned}\lambda_\eta^*(\eta,d) &= -\frac{r(\eta)\left(1+\left(\frac{r'(\eta)}{r(\eta)}\right)^2\right)}{2\left(1+2\left(\frac{r'(\eta)}{r(\eta)}\right)^2-\frac{r''(\eta)}{r(\eta)}-\frac{r(\eta)}{2d}\left(1+\left(\frac{r'(\eta)}{r(\eta)}\right)^2\right)\right)}\ ,\\ \lambda_\phi^*(\eta,d) &= -\frac{r(\eta)\left(1+\left(\frac{r'(\eta)}{r(\eta)}\right)^2\right)\sin\eta}{2\left(\sin\eta-\cos\eta\frac{r'(\eta)}{r(\eta)}-\sin\eta\frac{r(\eta)}{2d}\left(1+\left(\frac{r'(\eta)}{r(\eta)}\right)^2\right)\right)}\ .\end{aligned} \tag{13}$$

d is the distance of the object point from the surface.

For the constant angular gain mirror, Eq. (1), we find

$$\lambda_\eta^*(\eta,d)=\frac{r(\eta)}{\alpha-1+\frac{r(\eta)}{d}}\ ,\quad \lambda_\phi^*(\eta,d)=\frac{r(\eta)\sin\eta}{\sin(\alpha\eta+2\gamma)-\sin\eta+\frac{r(\eta)}{d}\sin\eta}\ . \tag{14}$$

Since, in general, λ_η^* and λ_ϕ^* are different, the reflective surface introduces a certain amount of image blur even locally.

Substituting Eq. (12) into (14), i.e. by using $d=d_\eta(\eta)$ and $d=d_\phi(\eta)$ for λ_η^* and λ_ϕ^* respectively, we obtain the locations of virtual images for the parallel light bundles considered before, including the refraction at the outer perspex surface:

$$\hat{\boldsymbol{v}}_\xi(\phi,\eta)=\boldsymbol{x}(\phi,\eta)+\lambda_\xi^*(\eta,d_\xi(\eta))\boldsymbol{e}(\phi,\eta)+(0,0,\Delta h)^\top\ . \tag{15}$$

where $\xi\in\{\eta,\phi\}$ indicates the two different groups of rays as before, and $\Delta h\approx h(1-n_p)$. The dashed curves in Fig. 3 b show vertical transects ($\phi=$ const.) of $\hat{\boldsymbol{v}}_\phi(\phi,\eta)$ (shown in green) and $\hat{\boldsymbol{v}}_\eta(\phi,\eta)$ (blue).

3.3 Refraction at the planar surface

Seen from the camera with camera angle $\theta\approx n_p\eta$, the virtual images appear closer due to refraction at the planar camera-facing perspex surface,

$$\boldsymbol{v}_\xi(\phi,\theta)\approx\left(\left(r(\tfrac{\theta}{n_p})+\lambda_\xi^*(\tfrac{\theta}{n_p},d_\xi(\tfrac{\theta}{n_p}))-\tfrac{h-\Delta h}{\cos(\frac{\theta}{n_p})}\right)\tfrac{\cos^2\theta}{n_p\cos^2(\frac{\theta}{n_p})}+\tfrac{h}{\cos\theta}\right)\boldsymbol{e}(\phi,\theta)\ . \tag{16}$$

$\boldsymbol{v}_\phi(\phi,\theta)$ and $\boldsymbol{v}_\eta(\phi,\theta)$ define the locations where the camera has to be focused at. As can be seen in Fig. 3 b, they do not lie in a plane and thus for large camera

[9] Of course, for $d\to\infty$ rays become parallel.

Workshop Proceedings of SIMPAR 2008
Intl. Conf. on SIMULATION, MODELING and PROGRAMMING for AUTONOMOUS ROBOTS
Venice(Italy) 2008 November,3-4
ISBN 978-88-95872-01-8
pp. 218-229

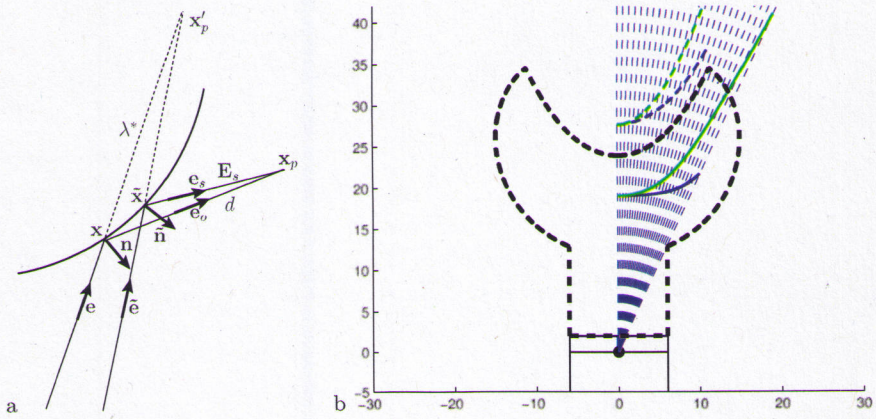

Fig. 3. a) Estimating the location of the virtual image of a point (with position vector $\boldsymbol{x}_p$). See appendix for details. b) Virtual image locations of the panoramic imaging system. The dashed curves show $\hat{\boldsymbol{v}}_\phi(\eta)$ (green) and $\hat{\boldsymbol{v}}_\eta(\eta)$ (blue) while the solid curves show $\boldsymbol{v}_\phi(\theta)$ (green) and $\boldsymbol{v}_\eta(\theta)$ (blue), i.e. the virtual images as they appear when "seen" from the camera.

apertures image blur will be visible.[10] In future work we will investigate to what extend this can be compensated by using additional optical elements [9].

4 Visual Navigation

In this section we describe the application of our imaging system to the robust estimation of egomotion.

4.1 Tracked Point Features in Image Sequences

We are able to track point features in grayscale images using a modified KLT tracker running in real-time on our laptop system. Fig. 4 depicts results of our real-time tracking system. The images originate from a test sequence taken with the system mounted on a high-precision KUKA robot that provides ground truth

[10] Similar to the derivation in [12], it can be shown that the blur region in the camera image — assuming a perfect camera lens, i.e. by neglecting blur caused by the camera lens — can be estimated by

$$A(z,\theta) \approx \frac{D^2 f^2}{z_\phi(\theta) z_\eta(\theta)} \frac{|z - z_\phi(\theta)||z - z_\eta(\theta)|}{z^2} \ , \tag{17}$$

$$z_\phi(\theta) := r_\phi(\theta)\cos\theta \ , \quad z_\eta(\theta) := r_\eta(\theta)\cos\theta \ , \tag{18}$$

where z is the distance the camera is focused at, D the size of the aperture, and f the focal length of the camera lens.

Workshop Proceedings of SIMPAR 2008
Intl. Conf. on SIMULATION, MODELING and PROGRAMMING for AUTONOMOUS ROBOTS
Venice(Italy) 2008 November,3-4
ISBN 978-88-95872-01-8
pp. 218-229

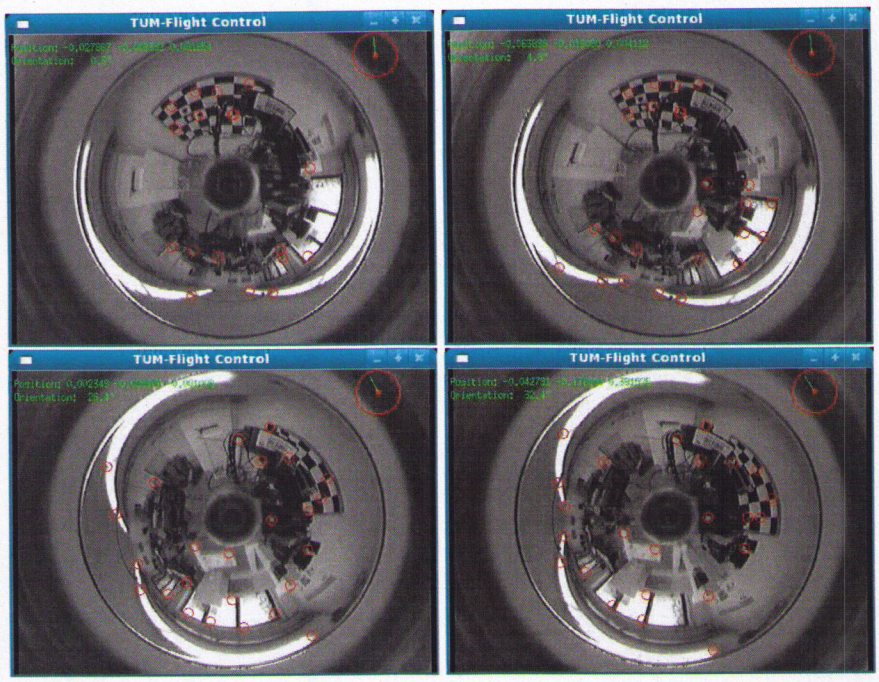

Fig. 4. Tracked sequence from the original video stream. The point features for tracking are obtained from a modified "`GoodFeaturesToTrack()`" routine of Intel's OpenCV image processing package. Image size is 480×352 pixels.

motion. The selected features are filtered with a mask representing the mirror and robot geometries that should not be used for motion estimation.

Since features move out of view of the sensor, we select new features to fill the camera image uniformly. This ensures a good condition number of the resulting localization. A sensitivity analysis is out of the scope of this paper and the reader can refer to [18] for details.

4.2 Abstraction of the Sensor Model

We use the "`cam2world`" function from the "OcamCalib" toolbox [16] to calculate the mapping functions $\phi(u_i^f, v_i^f)$ (azimuth) and $\varepsilon(u_i^f, v_i^f)$ (elevation) from the pixel values (u_i^f, v_i^f) in the camera image. Fig. 5 shows the almost linear relationship between the distance from the image center $\rho = \sqrt{u^2 + v^2}$ and the elevation angle ε.[11]

[11] The average mean reprojection error of checkerboard corners (averaged over 12 pictures) was 0.4636 pixel (min: 0.3428 pixel, max: 0.5405 pixel). The parameters of the

Workshop Proceedings of SIMPAR 2008
Intl. Conf. on SIMULATION, MODELING and PROGRAMMING for AUTONOMOUS ROBOTS
Venice(Italy) 2008 November,3-4
ISBN 978-88-95872-01-8
pp. 218-229

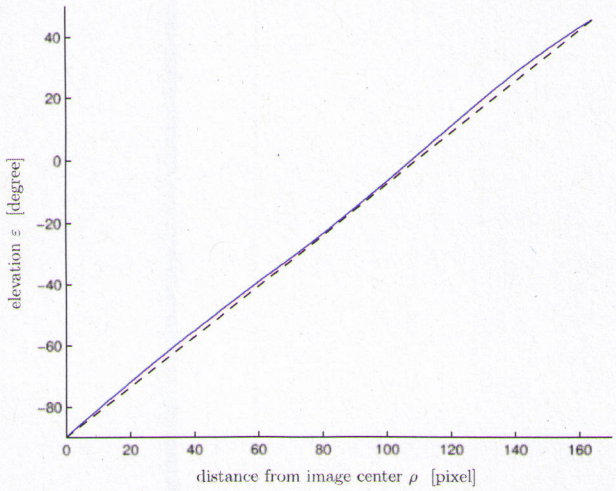

Fig. 5. Calibration of the imaging system with the "OcamCalib" toolbox confirms the almost linear mapping between the distance from the image center and the elevation angle (shown for azimuth angle $\phi = 0$, the curves for different azimuth angles are virtually identical). The dashed line shows $\varepsilon = 0.8208°/\text{pixel} \times \rho$.

The abstraction of our mirror system to a single view-point camera allows to use our already presented navigation algorithms that apply directly to raw camera images after a correction for the imaging properties.

4.3 Navigation Alternatives

Z_∞ Navigation. We presented already in [19] an alternative for direct calculation of the motion parameters from two images with given point correspondences between them. For large viewing areas in image sequences a separation of features in distant and close ones is possible. This seperation allows direct calculation of the resulting rotation matrix. A compensation of the rotation can be applied to all correspondences resulting in a direct estimation of the translation up to an unknown scale. This method also allows to estimate the accuracy of the computed motion values [19].

VGPS *Navigation Method.* For indoor navigation with just close features surrounding the sensor, we apply our VGPS method [20] to estimate the motion of the camera between frames.

We plan to add an extended experimental validation of the already acquired navigation data with ground-truth from a high precision manipulator in an extended version of this paper.

polynomial $f(\rho) = a_0 + a_1\rho + a_2\rho^2 + a_3\rho^3 + a_4\rho^4$ used in the calibration model were estimated to be $a_0 = -63.2$, $a_1 = 0$, $a_2 = 0.003$, $a_3 = 5.3 \times 10^{-7}$, $a_4 = 1.95 \times 10^{-7}$.

Workshop Proceedings of SIMPAR 2008
Intl. Conf. on SIMULATION, MODELING and PROGRAMMING for AUTONOMOUS ROBOTS
Venice(Italy) 2008 November,3-4
ISBN 978-88-95872-01-8
pp. 218-229

Appendix

We will present the major steps in the derivation of (13) by considering two light rays that start from a single point p, see Fig. 3 a. The first ray, the "principal ray", hits the mirror surface at $\boldsymbol{x}(\phi,\eta)$ and runs, after reflection, along the vector $-\boldsymbol{e}(\phi,\eta)$ through the origin of the coordinate system. For a reflective surface defined by $\boldsymbol{x}(\phi,\eta) = r(\eta)\boldsymbol{e}(\phi,\eta)$ as in Eqs. (1), (2), the position of p can thus be described by

$$\boldsymbol{x}_p = \boldsymbol{x}(\phi,\eta) + d\,\boldsymbol{e}_o(\phi,\eta) \ , \tag{19}$$

where $\boldsymbol{e}_o := \boldsymbol{e} - 2(\boldsymbol{n}\boldsymbol{e})\boldsymbol{n}$ is a direction vector[12], obtained from reflecting $\boldsymbol{e}$ at the mirror surface; $\boldsymbol{n}$ is the local normal vector in point $\boldsymbol{x}$.[13] The second ray considered runs along $-\boldsymbol{e}_s = -(\tilde{\boldsymbol{e}} - 2(\tilde{\boldsymbol{n}}\tilde{\boldsymbol{e}})\tilde{\boldsymbol{n}})$ and hits the surface at point $\tilde{\boldsymbol{x}} = \boldsymbol{x}(\phi+\Delta\phi,\eta+\Delta\eta)$, shifted in a direction defined by ψ, i.e. $\Delta\phi = \Delta\mu\sin\psi$ and $\Delta\eta = \Delta\mu\cos\psi$.

We will use Taylor expansion up to second order to determine the virtual image of p,

$$\boldsymbol{x}'_p = \boldsymbol{x}(\phi,\eta) + \lambda^*\boldsymbol{e}(\phi,\eta) = (r(\eta)+\lambda^*)\boldsymbol{e}(\phi,\eta) \ . \tag{20}$$

λ^* gives the distance from $\boldsymbol{x}$ along $\boldsymbol{e}$ where the two rays after reflection at the mirror have their smallest distance from each other. It can be easily shown that

$$\lambda^* = \tfrac{(\tilde{\boldsymbol{x}}-\boldsymbol{x})((\boldsymbol{e}\tilde{\boldsymbol{e}})\tilde{\boldsymbol{e}}-\boldsymbol{e})}{(\boldsymbol{e}\tilde{\boldsymbol{e}})^2-1} \ . \tag{21}$$

Next, we estimate $\tilde{\boldsymbol{e}}$ given by

$$\tilde{\boldsymbol{e}} = \boldsymbol{e}_s - 2(\tilde{\boldsymbol{n}}\boldsymbol{e}_s)\tilde{\boldsymbol{n}} \ . \tag{22}$$

From Fig. 3 a, we see that

$$\begin{aligned}
\boldsymbol{e}_s &= \tfrac{\boldsymbol{E}_s}{|\boldsymbol{E}_s|} = \tfrac{d\boldsymbol{e}_o-(\tilde{\boldsymbol{x}}-\boldsymbol{x})}{d\sqrt{e_o^2-2\frac{(\tilde{\boldsymbol{x}}-\boldsymbol{x})\boldsymbol{e}_o}{d}+\frac{(\tilde{\boldsymbol{x}}-\boldsymbol{x})^2}{d^2}}} \approx \boldsymbol{e}_o + \boldsymbol{\Delta e}_s + \boldsymbol{\Delta^2 e}_s \ , \\
\boldsymbol{\Delta e}_s &:= \tfrac{(\boldsymbol{e}_o\boldsymbol{\Delta x})\boldsymbol{e}_o-\boldsymbol{\Delta x}}{d} \ , \\
\boldsymbol{\Delta^2 e}_s &:= \tfrac{(\boldsymbol{e}_o\boldsymbol{\Delta^2 x})\boldsymbol{e}_o-\boldsymbol{\Delta^2 x}}{d} + \tfrac{3(\boldsymbol{e}_o\boldsymbol{\Delta x})^2\boldsymbol{e}_o-2(\boldsymbol{e}_o\boldsymbol{\Delta x})\boldsymbol{\Delta x}-(\boldsymbol{\Delta x})^2\boldsymbol{e}_o}{2d^2} \ .
\end{aligned} \tag{23}$$

Here and in the following, we use for $\boldsymbol{z} \in \{\boldsymbol{x},\boldsymbol{n}\}$ the approximation

$$\tilde{\boldsymbol{z}} \approx \boldsymbol{z} + \boldsymbol{\Delta z} + \boldsymbol{\Delta^2 z} \ , \tag{24}$$

with the abbreviations

$$\boldsymbol{\Delta z} := \tfrac{\partial \boldsymbol{z}}{\partial\phi}\Delta\phi + \tfrac{\partial \boldsymbol{z}}{\partial\eta}\Delta\eta \ , \quad \boldsymbol{\Delta^2 z} := \tfrac{1}{2}\tfrac{\partial^2 \boldsymbol{z}}{\partial\phi^2}\Delta\phi^2 + \tfrac{\partial^2 \boldsymbol{z}}{\partial\phi\partial\eta}\Delta\eta\Delta\phi + \tfrac{1}{2}\tfrac{\partial^2 \boldsymbol{z}}{\partial\eta^2}\Delta\eta^2 \ .$$

[12] All direction vectors ($\boldsymbol{e}$, $\tilde{\boldsymbol{e}}$, $\boldsymbol{n}$, ...) are assumed to have unit length.

[13] $\boldsymbol{n}$ is given by $\frac{\frac{\partial \boldsymbol{x}}{\partial\phi}\times\frac{\partial \boldsymbol{x}}{\partial\eta}}{\left\|\frac{\partial \boldsymbol{x}}{\partial\phi}\times\frac{\partial \boldsymbol{x}}{\partial\eta}\right\|}$.

Workshop Proceedings of SIMPAR 2008
Intl. Conf. on SIMULATION, MODELING and PROGRAMMING for AUTONOMOUS ROBOTS
Venice(Italy) 2008 November,3-4
ISBN 978-88-95872-01-8
pp. 218-229

Substituting (23) into Eq. (22), we obtain

$$\begin{aligned}
\tilde{\boldsymbol{e}} &= \boldsymbol{e}_s - 2(\tilde{\boldsymbol{n}}\boldsymbol{e}_s)\tilde{\boldsymbol{n}} \approx \boldsymbol{e} + \boldsymbol{\Delta e} + \boldsymbol{\Delta^2 e} \ , \\
\boldsymbol{\Delta e} &:= \boldsymbol{\Delta e}_s - 2\Big((\boldsymbol{n}\boldsymbol{\Delta e}_s)\boldsymbol{n} + (\boldsymbol{\Delta n}\boldsymbol{e}_o)\boldsymbol{n} + (\boldsymbol{n}\boldsymbol{e}_o)\boldsymbol{\Delta n}\Big) \ , \\
\boldsymbol{\Delta^2 e} &:= \boldsymbol{\Delta^2 e}_s - 2\Big((\boldsymbol{n}\boldsymbol{\Delta^2 e}_s)\boldsymbol{n} + (\boldsymbol{\Delta n}\boldsymbol{\Delta e}_s)\boldsymbol{n} + (\boldsymbol{n}\boldsymbol{\Delta e}_s)\boldsymbol{\Delta n} \\
&\qquad + (\boldsymbol{\Delta^2 n}\boldsymbol{e}_o)\boldsymbol{n} + (\boldsymbol{\Delta n}\boldsymbol{e}_o)\boldsymbol{\Delta n} + (\boldsymbol{n}\boldsymbol{e}_o)\boldsymbol{\Delta^2 n}\Big) \ .
\end{aligned}$$

This leads to the second order approximation of Eq. (21),

$$\lambda^* \approx \frac{\boldsymbol{\Delta x}\boldsymbol{\Delta e}}{2\boldsymbol{e}\boldsymbol{\Delta^2 e}} \ , \tag{25}$$

and, after some lengthy algebraic manipulations, we finally have

$$\begin{aligned}
\lambda^* &\approx -\tfrac{1}{2}r(\eta)\Big(1 + (\tfrac{r'}{r})^2\Big)\tfrac{\Delta\eta^2 g(\eta) + \Delta\phi^2 h(\eta)\sin\eta}{\Delta\eta^2 g(\eta)^2 + \Delta\phi^2 h(\eta)^2} \ , \\
g(\eta) &:= 1 + 2(\tfrac{r'}{r})^2 - \tfrac{r''}{r} - \tfrac{r}{2d}\big(1 + (\tfrac{r'}{r})^2\big) \ , \\
h(\eta) &:= \big(\sin\eta - \cos\eta\tfrac{r'}{r}\big) - \sin\eta\tfrac{r}{2d}\big(1 + (\tfrac{r'}{r})^2\big) \ .
\end{aligned} \tag{26}$$

Substituting $\Delta\eta = \Delta\mu\cos\psi$ and $\Delta\phi = \Delta\mu\sin\psi$, where ψ defines the direction of the shift between the two points $\boldsymbol{x}$ and $\tilde{\boldsymbol{x}}$ on the mirror, we obtain

$$\lambda^* \approx \tfrac{1}{2}r(\eta)\Big(1 + (\tfrac{r'}{r})^2\Big)\tfrac{\cos^2\psi g(\eta) + \sin^2\psi h(\eta)\sin\eta}{\cos^2\psi g(\eta)^2 + \sin^2\psi h(\eta)^2} \ . \tag{27}$$

The extremal values of λ^* with respect to $\chi := \cos^2\psi = 1 - \sin^2\psi$ are for $\chi = 0$ and $\chi = 1$,[14]

$$\lambda^*_\eta := -\tfrac{1}{2}r(\eta)\Big(1 + (\tfrac{r'}{r})^2\Big)\tfrac{1}{g(\eta)} \ , \quad \lambda^*_\phi := -\tfrac{1}{2}r(\eta)\Big(1 + (\tfrac{r'}{r})^2\Big)\tfrac{\sin\eta}{h(\eta)} \ , \tag{28}$$

already defined in (13).

References

1. Haehnel, D., Burgard, W., Thrun, S.: Learning compact 3d models of indoor and outdoor environments with a mobile robot. In: Robotics and Autonomous Systems. Volume 44. (2003) 15–27
2. Burgard, W., Fox, D., Hennig, D., Schmidt, T.: Estimating the absolute position of a mobile robot using position probability grids. In: Proceeding of the 14th National Conference on Artificial Intelligence (AAAI-96). (1996)
3. Fermüller, C., Aloimonos, Y.: Ambiguity in structure from motion: Sphere versus plane. International Journal of Computer Vision **28** (1998) 137–154
4. Gurdan, D., Stumpf, J., Achtelik, M., Doth, K.M., Hirzinger, G., Rus, D.: Energy-efficient autonomous four-rotor flying robot controlled at 1 khz. In: ICRA 2007. (2007) 361–366

[14] $f(\chi) := \frac{\partial\lambda^*}{\partial\chi} = \frac{h(\eta)^2 g(\eta) - g(\eta)^2 h(\eta)\sin\eta}{\big(\chi g(\eta)^2 + (1-\chi)h(\eta)^2\big)^2}$ has no root, and λ^* has no pole (since the denominator is positive) in $0 < \chi < 1$.

Workshop Proceedings of SIMPAR 2008
Intl. Conf. on SIMULATION, MODELING and PROGRAMMING for AUTONOMOUS ROBOTS
Venice(Italy) 2008 November,3-4
ISBN 978-88-95872-01-8
pp. 218-229

5. Menegatti, E., Zoccarato, M., Pagello, E., Ishiguro, H.: Image-based monte carlo localisation with omnidirectional images. Robotics and Autonomous Systems **48** (2004) 17–30
6. Goedemé, T., Nuttin, M., Tuytelaars, T., Gool, L.V.: Omnidirectional vision based topological navigation. International Journal of Computer Vision **74** (2007) 219–236
7. Möller, R.: Local visual homing by warping of two-dimensional images. Robotics and Autonomous Systems (in press) (2008)
8. Chahl, J., Srinivasan, M.: Reflective surfaces for panoramic imaging. Applied Optics **36** (1997) 8275–8285
9. Baker, S., Nayar, S.K.: A theory of single-viewpoint catadioptric image formation. International Journal of Computer Vision **35** (1999) 175–196
10. Stürzl, W., Soccol, D., Zeil, J., Boeddeker, N., Srinivasan, M.: A rugged, obstruction-free, mirror-lens combination for panoramic imaging. Applied Optics (accepted) (2008)
11. Ishiguro, H.: Development of low-cost compact omnidirectional vision sensors. In Benosman, R., Kang, S., eds.: Panoramic Vision. Springer (2001) 23–38
12. Stürzl, W., Dahmen, H.J., Mallot, H.: The quality of catadioptric imaging – application to omnidirectional stereo. In Pajdla, T., Matas, J., eds.: ECCV 2004. Volume 3021 of *LNCS*., Springer (2004) 614–627
13. Swaminathan, R., Grossberg, M., Nayar, S.: Caustics of catadioptric cameras. In: ICCV 2001. (2001) 2–9
14. Swaminathan, R., Grossberg, M.D., Nayar, S.K.: Non-single viewpoint catadioptric cameras: Geometry and analysis. International Journal of Computer Vision **66** (2006) 211–229
15. Ieng, S., Benosman, R.: Geometric construction of the caustic curves for catadioptric sensors. In Daniilidis, K., Klette, R., eds.: Imaging Beyond the Pinhole Camera, Kluwer Academic Publisher (2006)
16. Scaramuzza, D., Martinelli, A., Siegwart, R.: A toolbox for easily calibrating omnidirectional cameras. In: IROS 2006. (2006) 5695–5701
17. Micusik, B., Pajdla, T.: Autocalibration & 3D reconstruction with non-central catadioptric cameras. In: CVPR 2004. (2004) 58–65
18. Burschka, D.: Collaborative Exploration with Dynamically Configurable Sensing Agents . In: ECCV 2008 Workshop on Vision in Action. (2008) to appear
19. Burschka, D., Mair, E.: Direct Pose Estimation with a Monocular Camera. Robot Vision (2008) 440–453
20. Burschka, D., Hager, G.D.: V-GPS – Image-Based Control for 3D Guidance Systems. In: Proc. of IROS. (October 2003) 1789–1795

Workshop Proceedings of SIMPAR 2008
Intl. Conf. on SIMULATION, MODELING and PROGRAMMING for AUTONOMOUS ROBOTS
Venice(Italy) 2008 November,3-4
ISBN 978-88-95872-01-8
pp. 218-229